JOURNAL OF MATERIALS SCIENCE **34** (1999) 1447–1460

# A comparison of strengthening mechanisms in rolled and axisymmetrically deformed Ti-20Y composites

A. M. RUSSELL, L. S. CHUMBLEY, F. C. LAABS, J. D. RUSSELL
*Ames Laboratory, Iowa State University, Ames, IA, USA 50011*
*E-mail: russell@iastate.edu*

Two Ti-20%Y metal-metal composites were deformation processed: one axisymmetrically and the other by rolling. The microstructures, preferred crystallographic orientations, and tensile strengths of each were measured periodically as the deformation progressed. The axisymmetrically deformed Ti matrix developed a $[10\bar{1}0]$ fiber texture, and the rolled composite acquired a texture with the $\langle 0001 \rangle$ tilted 31° from the sheet normal toward the transverse direction with $[10\bar{1}0]$ parallel to the rolling direction. The orientations of the $\{10\bar{1}0\}\langle 11\bar{2}0 \rangle$ and $(0002)\langle 11\bar{2}0 \rangle$ slip systems in Ti with these textures were used in conjunction with the maximum possible slip distances for dislocation travel in each specimen to demonstrate that the axisymmetrically deformed material should be stronger than the rolled material for composites of equal phase thickness and spacing. The strengths of the two composites measured in this study were compared at similar microstructural phase sizes and spacings, and the axisymmetrically deformed composite was indeed found to be somewhat stronger, although the difference in strengths was not large. © *1999 Kluwer Academic Publishers*

## 1. Introduction

### 1.1. Deformation processed metal-metal composites

During the past two decades, a new class of metal matrix-metal second phase composites has been developed with extraordinary mechanical and electrical properties [1–3]. The most thoroughly studied of these metal-metal composites are the Cu-X composites which have a Cu matrix containing 10% to 30% element X (where X is a body-centered cubic (BCC) metal immiscible in Cu such as Nb, V, Ta, Cr, or Fe). When severely deformed, they develop a nanometer-scale microstructure of X filaments (when deformed by drawing) or lamellae (by rolling) in the Cu matrix. The Cu-20%Nb system is the most thoroughly studied of these deformation-processed metal-metal composites (DMMCs) and has ultimate tensile strengths exceeding 2000 MPa after deformation to a true strain of 12 [4]. The Cu-X composites are remarkably ductile, which allows cast or powder processed starting billets to be deformed to as much as an 800-fold reduction in diameter. Such reductions in diameter produce a proportional reduction in the thickness and spacing of the Cu and X phases. Thus, an as-cast billet of Cu-20Nb containing Nb dendrites of average thickness 4 $\mu$m may be deformation processed at room temperature into a wire with Nb filaments averaging 7 nm thick [5]. Such *in-situ* processed composites have strengths substantially higher than those of any other Cu alloy. Debate continues on the mechanism(s) which account for the very high strengths of the Cu-X composites [6–10], but discussion centers around the role of the nanofilamentary X structure in impeding propagation and motion of dislocations in both the Cu and X phases. More recently studies have been conducted on DMMCs where the matrix metal was Ti, Mg, Al, Sc, or Au rather than Cu [11–16].

In both Cu matrix and non-Cu matrix systems, it has been observed that DMMC's produced by axisymmetric deformation (e.g. extrusion, swaging, drawing) are stronger at equivalent levels of true strain and phase spacing than DMMCs produced by rolling [12, 17]. In this study, DMMCs were produced from arc-melted 80 vol% Ti-20 vol% Y (Ti-20Y) specimens to provide a comparison of the strengths produced by these differing deformation methods. One Ti-20Y specimen was axisymmetrically deformed to a true strain of 7.27. In axisymmetric deformation, the true strain ($\eta$) can be calculated from $\eta =$ ln [initial cross sectional area/final cross sectional area]. A second Ti-20Y specimen was deformed by rolling to a true strain of 6.17. Effective true strain ($\eta$) for rolling deformation can be calculated using the relation between initial thickness ($t_0$) and final thickness ($t_f$):

$$\eta = \left(\frac{2}{\sqrt{3}}\right) \ln\left(\frac{t_0}{t_f}\right) \tag{1}$$

Both specimens' tensile strengths, phase spacings, and crystallographic textures were measured at various $\eta$

0022–2461 © *1999 Kluwer Academic Publishers*

levels to study the interrelationships of these factors in rolled and axisymmetrically deformed material.

### 1.2. Preferred orientations in deformed titanium and yttrium

The preferred orientation of pure $\alpha$-Ti rolled sheet is a 20° to 40° tilt of the $\langle 0001\rangle$ from the sheet normal toward the transverse direction with a $[10\bar{1}0]$ parallel to the rolling direction [18]. The preferred orientation of axisymmetrically deformed pure $\alpha$-Ti is a $[10\bar{1}0]$ fiber texture [19]. These textures result from the two slip systems active in Ti at room temperature. These were first reported by Anderson, Jillson, and Dunbar [20], who found that the critical resolved shear stress (CRSS) for slip in the $\langle 11\bar{2}0\rangle$ direction on the (0002) basal plane is 110 MPa, and the CRSS for slip in the $\langle 11\bar{2}0\rangle$ direction on the $\{10\bar{1}0\}$ first order prism planes is 50 MPa. Thus, the Ti unit cell is oriented for easiest slip when it lies in an orientation with a Schmid factor near 0.5 for the first order prism plane slip system, while still permitting cross slip on the basal plane. Twinning is sometimes observed in plastically deformed Ti as well.

No report was found in the literature for preferred orientation of rolled Y. However, Y is known to deform [21] with the same slip systems as those of Ti: primary slip on the $\{10\bar{1}0\}\langle 11\bar{2}0\rangle$ and secondary slip on the $(0002)\langle 11\bar{2}0\rangle$, and Y has a low c/a ratio (1.571), so rolled and axisymmetrically deformed pure $\alpha$-Y might be expected to acquire the same preferred crystallographic orientation as other low c/a ratio hexagonal close-packed (HCP) metals (e.g. Ti, Zr, Hf, Be) [19].

## 2. Experimental procedures

### 2.1. Material preparation and deformation processing

A cylindrical drop cast billet of 80 vol % Ti and 20 vol % Y was prepared for the rolling experiments; it had a mass of 4.14 kg, diameter 98 mm, and length 122 mm. Two flats were milled on the cast billet to give an effective thickness of 81 mm prior to the first rolling pass. A second drop cast cylindrical billet of 80 vol % Ti and 20 vol % Y was prepared for the axisymmetric deformation experiments; it had a mass of 1.78 kg, diameter 74 mm, and length 92 mm. The Ti sponge used to make these castings had a 99.9% metals basis purity (170 wt ppm O, 6 wt ppm N, and 81 wt ppm C), and the Y had a 99.8% metals basis purity (976 wt ppm O, 103 wt ppm N, and 102 wt ppm C).

The specimen for axisymmetric deformation was welded into an evacuated steel can and extruded at 1073 K through a 3 : 1 reducing die to $\eta = 2.25$. The extruded specimens, still within steel outer sleeves, were then swaged at room temperature. Swaging was performed in stages with a 60% reduction in cross sectional area by swaging followed by a 30-min stress-relief anneal in air at 973 K; this was in turn followed by another 60% reduction and another stress-relief anneal at 973 K, and so forth until the specimen had been reduced to a 2.0 mm diameter ($\eta = 7.27$).

The other cast specimen was rolled at 973 K with a 10% reduction in thickness for each pass to a thickness of 7.62 mm ($\eta = 2.72$). The outer 0.5 mm surface of the rolled plate was milled away to remove material with higher O and N content acquired during hot rolling in air. The plate was then cut into pieces that were wire brushed to further clean their surfaces and stacked seven-high inside a large Inconel can. The Inconel can was welded shut in an Ar-filled glove box. The canned stack of plates was then rolled at 973 K with a 10% reduction in thickness for each pass. The seven pieces roll-bonded to form a single plate with total true strain of 5.28. A portion of this $\eta = 5.28$ plate was then cold-rolled to $\eta = 6.17$.

Coupons were removed from the specimens at intermediate stages of deformation processing for tensile testing, scanning electron microscope (SEM) and transmission electron microscope (TEM) examination of the microstructure, and texture analysis.

### 2.2. Tensile testing procedures and ductility measurements

Tensile testing procedures for the larger specimens followed American Standards for Testing of Materials (ASTM) Standard E8. Specimens too small to conform to the standard dimensions were made with the same proportions as those prescribed by ASTM Standard E8. Four tensile specimens were tested for each condition, and the mean values are reported. Accurate determination of yield strength was not possible for the high $\eta$, axisymmetrically deformed specimens since they were too small to permit use of an extensometer. In the case of rolled material, two specimens were cut with the tensile axis parallel to the rolling direction, and two specimens were cut with the tensile axis perpendicular to the rolling direction. Ductility was calculated for each specimen by measuring the area of the fracture surface in a traveling microscope and comparing that area to the original cross sectional area of the specimen to calculate the percent reduction in area at the fracture surface.

### 2.3. Specimen preparation for SEM and TEM examination

SEM specimens were prepared by ordinary metallographic techniques and examined in an unetched condition. The large disparity in atomic number between Ti and Y provided strong contrast in back-scattered electron imaging. TEM specimens were thinned by ion milling on a liquid nitrogen chilled stage. A Philips CM30 S/TEM operated at 300 kV was used for all TEM micrography. For the as-cast samples, quantitative stereology [22] was used to measure mean free distance between dendrites. In the deformation processed materials, phase spacing determinations were made by measuring phase thicknesses across their short dimension and averaging these values.

### 2.4. Texture analysis

Metallographic specimens were examined for preferred orientation by both X-ray texture analysis and back-scattered electron orientation imaging microscopy (OIM). The mechanically polished specimens were electropolished in perchloric acid to remove the surface layer deformed by mechanical polishing. OIM specimens were then ion beam milled to remove the surface layer reactant products remaining after electropolishing.

X-ray texture pole figures were acquired using Mo X-rays, a 5 mm sample lateral oscillation and a 5° per spiral $\varphi$ (tilting) pitch. A 5-s sampling time was used with a 7.5° step in $\phi$ (rotation) between samplings. Measurements were made over the range $0° \leq \varphi \leq 80°$. OIM pole figures were acquired using a specimen tilt of 70° and electron beam energy of 20 kV to produce electron backscattered Kikuchi patterns that were detected using a TSL OIM unit mounted on a field emission AmRay 1845 SEM. The respective Euler angles are deduced automatically for each pixel in the image, and the corresponding preferred orientation pole figures are mapped on the basis of the associated orientation distribution function.

## 3. Results

### 3.1. The effect of deformation on microstructure and mechanical properties

Both the extruded and rolled composites displayed progressively finer microstructures with increasing amounts of deformation. The dendritic as-cast microstructure is typical of two metals that are miscible in the liquid state but immiscible in the solid state (Fig. 1).

In the axisymmetrically deformed composite, initial hot extrusion changed the original dendritic structure

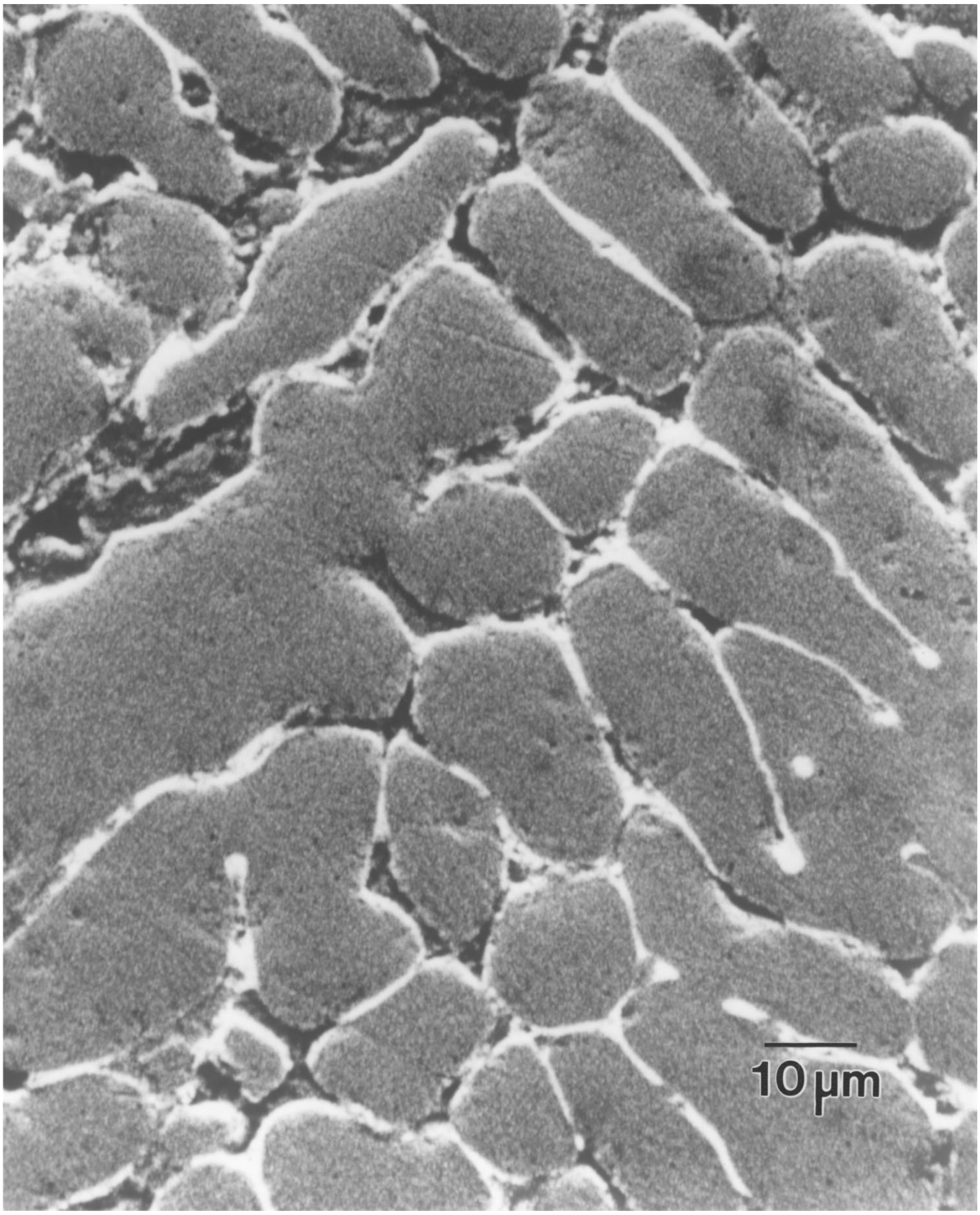

*Figure 1* SEM back-scattered electron micrograph of Ti-20Y as cast ($\eta = 0$). The gray matrix is Ti, and the lighter dendrites are Y. Some Y areas have corroded during metallographic preparation.

*Figure 2* TEM micrograph of Ti-20Y axisymmetrically deformed to $\eta = 5.03$. The imaging contrast in this micrograph renders the Y phase dark gray and the Ti matrix light gray. This transverse section of the specimen shows a point view of the rod axis and a true length view of the rod diameter.

to a filamentary structure similar to that observed in Cu-X *in-situ* composites. This is illustrated in Fig. 2, where the microstructure is shown after the 1073 K extrusion to $\eta = 2.25$ and cold swaging to $\eta = 5.03$. The size and spacing of the kinked, ribbon-shaped filaments decreased with continuing deformation up through $\eta = 7.27$. In the rolled composite, initial hot work changed the original dendritic structure to a lamellar structure. The size and spacing of the lamellae decreased with continuing rolling at 973 K to $\eta = 5.28$ and cold rolling up to $\eta = 6.17$ (Fig. 3).

Table I shows the changes in mechanical properties and phase size that resulted from the deformation processing. As would be expected, deformation processing substantially increased the ultimate tensile strength (UTS) of both Ti-20Y composites. In the rolled material, the strength of the specimens cut with the tensile axis parallel to the rolling direction was not appreciably different from the strength of the specimens cut with the tensile axis perpendicular to the rolling direction. Although the sample size (four specimens) is too small to calculate a statistically significant standard deviation, the UTS values were all within ±8% of the mean value reported in Table I, and most were within ±2%.

The axisymmetrically deformed Ti-20Y composite UTS increased 3.9 times as $\eta$ increased from 0 to 7.27. This is similar to the UTS increase seen in axisymmetrically deformed Cu-20Nb over the same range of $\eta$. The rolled Ti-20Y composite increased 2.5 times in UTS as $\eta$ increased from 0 to 6.17.

The hot rolling deformation between $\eta = 0$ and 5.28 caused a disproportionately small reduction in phase size. Equation 1 predicts that a net true strain by rolling of 5.28 would reduce phase thickness by a factor of nearly 100. However, a reduction in phase thickness of only 6.5 times is seen in the data in Table I. This

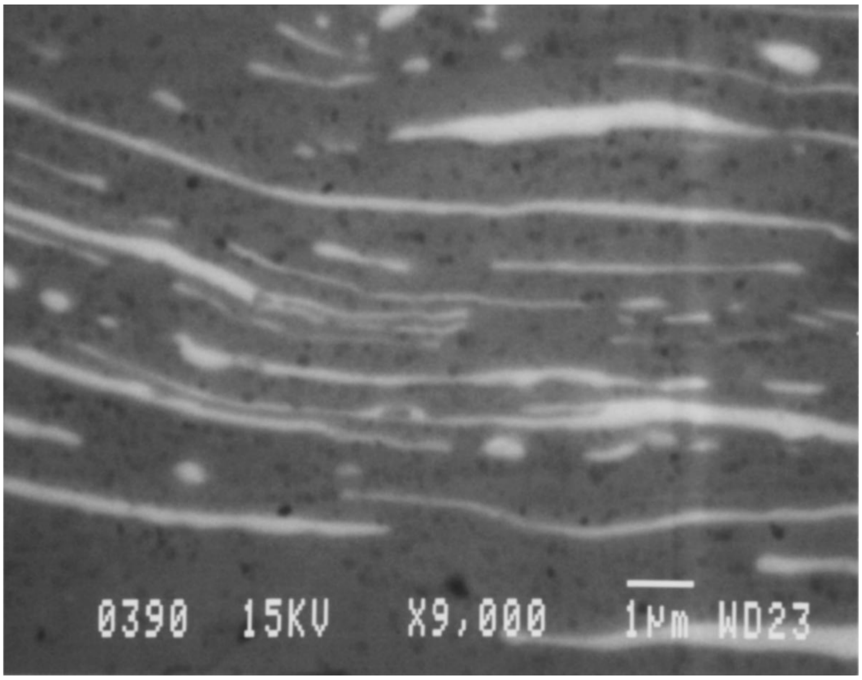

*Figure 3* SEM micrograph of Ti-20Y rolled to $\eta = 6.17$. This back-scattered electron image shows the Y phase as light gray lamellae in a dark gray Ti matrix. This transverse section of the specimen shows a point view of the rolling direction. The appearance of rolled specimens cut to show a true length view of the rolling direction is essentially identical.

TABLE I Ultimate tensile strength, ductility, and phase size measurements for tensile specimens of Ti-20Y deformed axisymmetrically and by rolling. UTS values shown are the average from four tensile specimens in each of the nine conditions

| Specimen | Ultimate tensile strength (MPa) | Ductility: Reduction in area at fracture surface | Mean Ti phase thickness ($\mu$m) | Mean Y phase thickness ($\mu$m) |
|---|---|---|---|---|
| Axisymmetrically deformed | | | | |
| Ti-20Y as-cast ($\eta = 0$) | 242 | 37% | 9.6 | 2.4 |
| Ti-20Y as-hot-extruded ($\eta = 2.25$) | 303 | 48% | 3.8 | 1.0 |
| Ti-20Y as-cold swaged ($\eta = 5.03$) | 655 | 45% | 0.59 | 0.17 |
| Ti-20Y as-cold swaged ($\eta = 6.82$) | 813 | 37% | NA | NA |
| Ti-20Y as-cold swaged ($\eta = 7.27$) | 949 | 42% | 0.16 | 0.041 |
| Rolled | | | | |
| Ti-20Y as-cast ($\eta = 0$) | 241 | 31% | 8.4 | 2.0 |
| Ti-20Y as-hot rolled ($\eta = 2.73$) | 350 | 58% | 2.9 | 0.67 |
| Ti-20Y as-hot rolled ($\eta = 5.28$) | 382 | 62% | 1.3 | 0.38 |
| Ti-20Y as-cold rolled ($\eta = 6.17$) | 609 | 30% | 0.56 | 0.15 |

may have resulted from diffusion-driven coarsening of the phases occurring simultaneously and in opposition to the phase size reduction from rolling. As the phase thickness decreases, the driving force for coarsening becomes much greater [23–25]; a similar effect was seen in a Sc-Ti DMMC hot rolled at 873 K [15]. The reduction in phase thickness seen for the cold rolling from $\eta = 5.28$ to 6.17 is close to that predicted by Equation 1. Other specimens of rolled Ti-20Y held at 973 K for periods similar to the time involved in hot rolling for this study showed extensive coarsening of the lamellae to cylindrical and spherical shapes. Unfortunately, rolling at lower temperatures does not provide sufficient ductility to avoid cracking the specimen.

It is particularly significant to note that the Ti and Y phase thicknesses are very nearly equal for the cases of axisymmetrically deformed material at $\eta = 5.03$ and rolled material at $\eta = 6.17$. This coincidence of phase thicknesses allowed a convenient comparison of the strengths of the two dissimilarly deformed composites, as discussed in Section 4.

### 3.2. Gas fusion analysis results

Oxygen and nitrogen have little effect on either strength or ductility in Y at the levels seen in these specimens [26]. However, O and N are powerful strengthening and embrittling agents in Ti [27], and for that reason the levels of these interstitial impurities were monitored by gas fusion analysis, which indicated that O content was maintained between 663 and 895 wt ppm and N content was maintained between 37 and 43 wt ppm throughout the course of the deformation processing. Such variations would have only minor effects on mechanical properties.

### 3.3. Texture measurements

Pole figures for the as-cast Ti-20Y specimens showed no significant texture. After deformation began, however, a strong $\langle 10\bar{1}0\rangle$ fiber texture was observed in both the Ti and Y phases of the axisymmetrically deformed Ti-20Y composite throughout the deformation processing range $2.25 \leq \eta \leq 7.27$ (Figs 4 and 5). The $\langle 10\bar{1}0\rangle$ fiber texture is normally observed in drawn

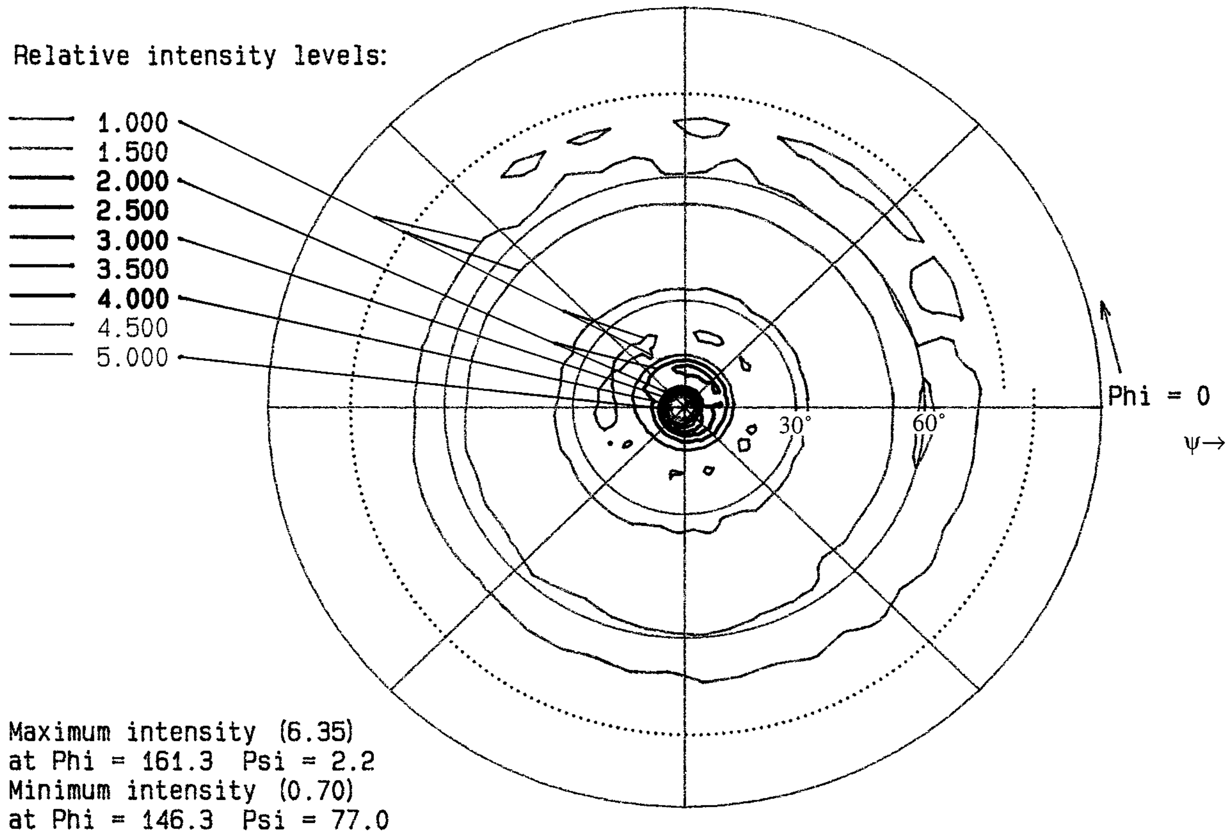

*Figure 4* X-ray diffraction pole figure (maximum $\psi = 80°$) for the $(10\bar{1}0)$ plane of the Ti phase axisymmetrically deformed to $\eta = 5.03$. The specimen was mounted transversely; a point view of the rod axis lies at the center of the pole figure. The "ideal" $\langle 10\bar{1}0\rangle$ fiber texture would yield a strong central peak of intensity and a weaker ring of intensity at $\psi = 60°$.

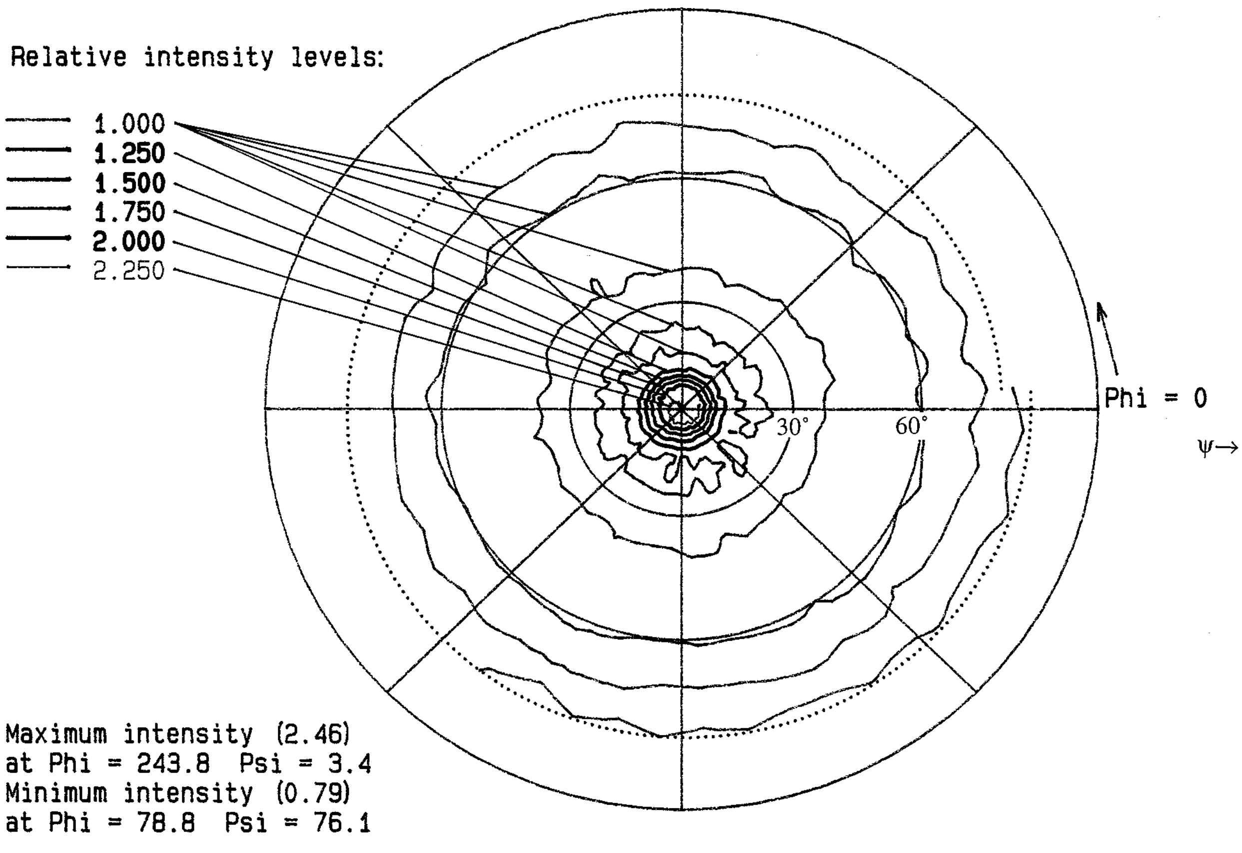

*Figure 5* X-ray diffraction pole figure (maximum $\psi = 80°$) for the $(10\bar{1}0)$ plane of the Y phase axisymmetrically deformed to $\eta = 5.03$. The specimen was mounted transversely; a point view of the rod axis lies at the center of the pole figure. Note that the texture is the same as that of the Ti phase shown in Fig. 4.

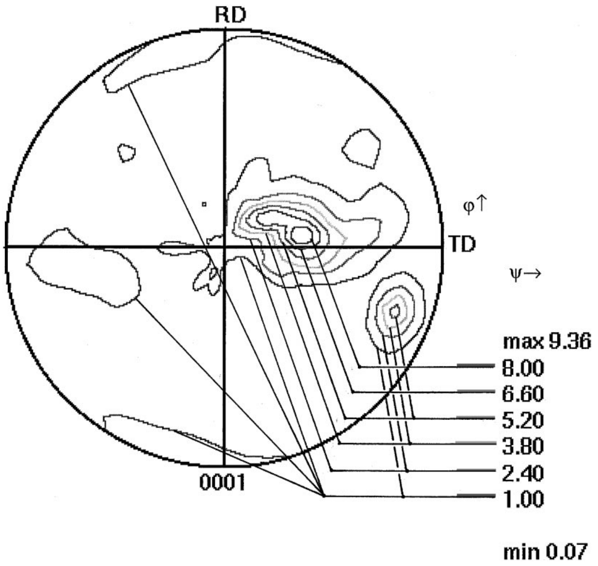

*Figure 6* Equal angle OIM pole figure (maximum $\psi = 90^\circ$) for the (0002) plane of the Ti phase of Ti-20Y rolled to $\eta = 6.17$. Rolling direction is labeled RD. The commonly observed texture of cold-rolled Ti is evident here, a 20° to 40° tilt of the $\langle 0001 \rangle$ toward the transverse direction (TD).

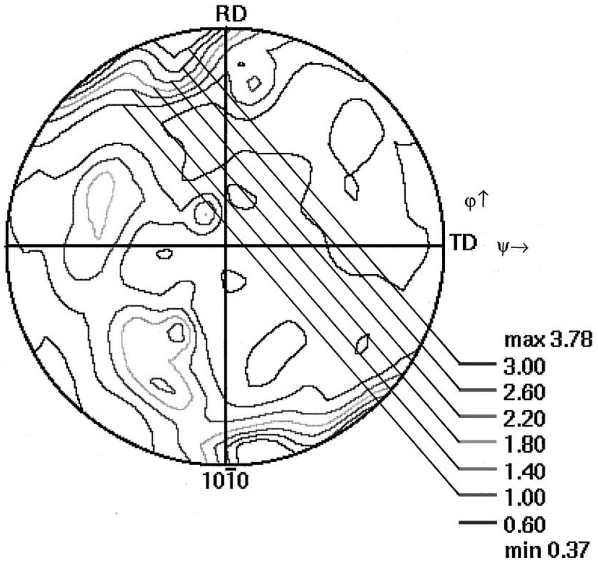

*Figure 7* Equal angle OIM pole figure (maximum $\psi = 90^\circ$) for the $(10\bar{1}0)$ plane of the Ti phase of Ti-20Y rolled to $\eta = 6.17$. Note that some $\langle 10\bar{1}0 \rangle$ directions are nearly parallel to the rolling direction (RD), which is consistent with the commonly observed texture of cold-rolled Ti.

Ti [19], and its occurrence in drawn Y has been less throughly studied [28] but seems a likely texture for Y since its c/a ratio is identical to that of Ti.

In the rolled Ti-20Y, the observed texture in the Ti matrix was a 31° tilt of the [0001] from the sheet plane approximately in the transverse direction. The $[10\bar{1}0]$ is approximately parallel to the rolling direction (Figs 6 and 7). This is the rolling texture usually seen in cold rolled Ti.

## 4. Discussion

### 4.1. Texture induced plane strain in both matrix and second phase of axisymmetrically deformed Ti-20Y

In the axisymmetrically deformed Ti-20Y composite, the observed $\langle 10\bar{1}0 \rangle$ fiber texture (Figs 8 and 9) in both the Ti and the Y phases limits each phase to plane strain. This results from the orientation of the two slip systems active in Ti (and presumably in Y as well) at room temperature.

With the large CRSS of 110 MPa in the $(0002)\langle 11\bar{2}0 \rangle$ slip system in Ti, it is not surprising that Ti textures to optimize slip on the $\{10\bar{1}0\}$ $\langle 11\bar{2}0 \rangle$ slip system, where the CRSS is lower at 50 MPa. It seems likely that Y, with the same low c/a ratio as Ti, behaves similarly. With the $\langle 10\bar{1}0 \rangle$ fiber texture observed for both Ti and Y in this experiment, applying Schmid's Law to calculate the shear stress for basal plane slip yields:

$$\tau_r = \sigma \cos\phi \cos\lambda = 0 \qquad (2)$$

where $\tau_r$ = the resolved shear stress on the given slip system, $\sigma$ = tensile stress, $\lambda$ = the angle between the rod axis and the slip direction (30° or 90°), and $\phi$ = the angle between the rod axis and the normal to the slip plane (90°). For the same $\langle 10\bar{1}0 \rangle$ fiber textured rod, $\tau_r$ for the $\{10\bar{1}0\}\langle 11\bar{2}0 \rangle$ slip system is:

$$\tau_r = \sigma \cos(60^\circ) \cos(30^\circ) = 0.433\sigma$$

A resolved shear stress of $0.433\sigma$ is near the maximum possible value of $0.5\sigma$, and this slip system must be

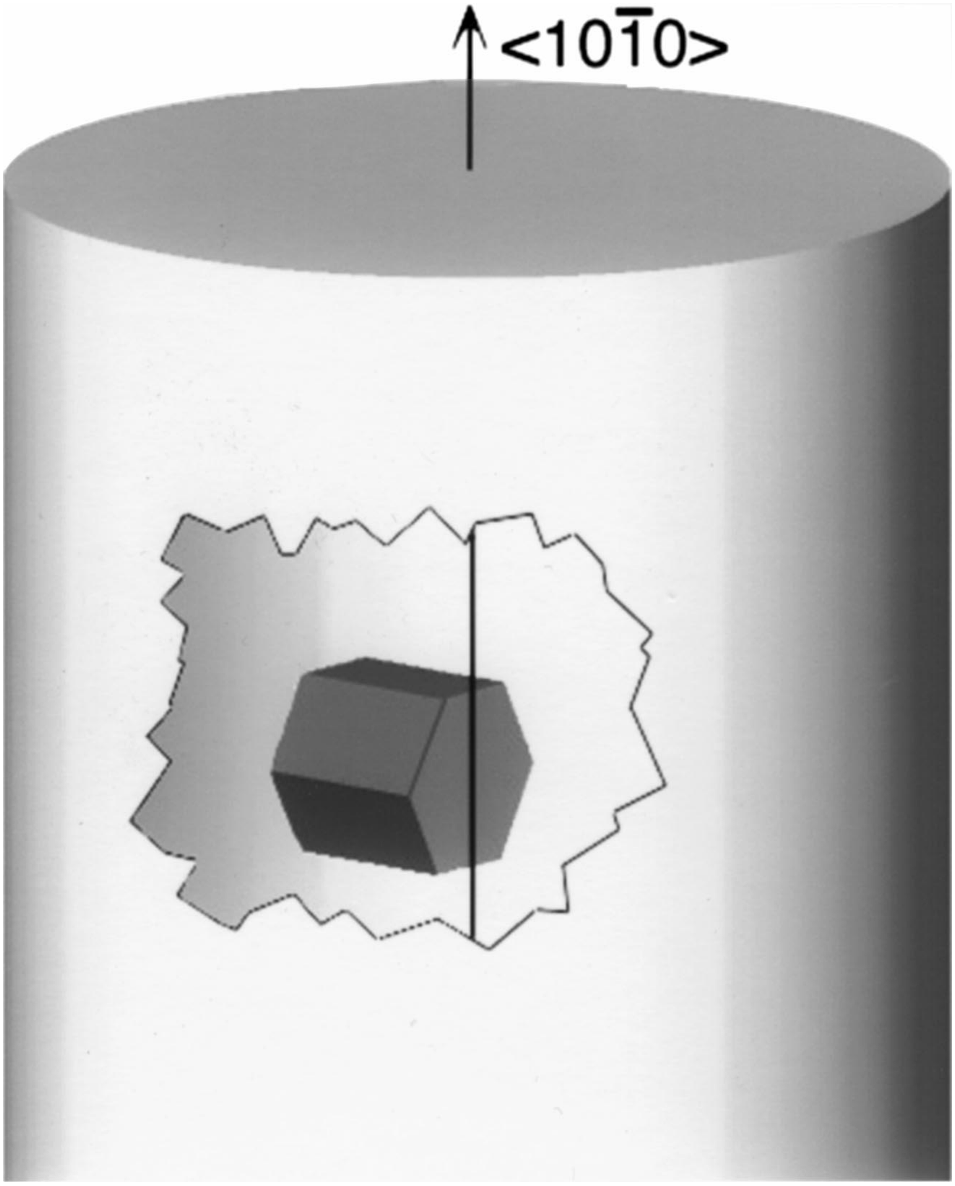

*Figure 8* Depiction of an HCP unit cell oriented with the $\langle 10\bar{1}0\rangle$ direction parallel to the rod axis of an axisymmetrically deformed specimen.

the dominant one in tensile testing of axisymmetrically deformed specimens with a $\langle 10\bar{1}0\rangle$ fiber texture. Basal slip would not occur at all during the onset of plastic flow in an ideal $\langle 10\bar{1}0\rangle$ fiber textured rod. Of course the texture is not "perfect"; some grains are oriented at angles other than the idealized texture, and basal slip would be possible in those grains with non-zero Schmid factors for the $(0002)\langle 11\bar{2}0\rangle$ slip system. But in most grains, the $\tau_r$ for basal slip would be much lower than the $\tau_r$ for slip on the $\{10\bar{1}0\}\langle 11\bar{2}0\rangle$ slip system.

In the rolled Ti-20Y composite, the observed texture presents a more complicated set of slip options, and both the $(0002)\langle 11\bar{2}0\rangle$ and $\{10\bar{1}0\}\langle 11\bar{2}0\rangle$ systems would be expected to experience substantial amounts of slip, as described in the following section.

### 4.2. Strength in rolled and axisymmetrically deformed Ti-20Y composites

One can make the somewhat simplistic assumption that all the Ti matrix grains in the axisymmetrically deformed composite are oriented in the position that shows the highest intensity on the pole figure in Fig. 4. Similarly it could be assumed that all the Ti matrix grains in the rolled composite are oriented in the position that shows the highest intensity on the pole figure in Fig. 6. For simplicity, the rolled texture in the following analysis is assumed to have the $\langle 0001\rangle$ inclined $30^\circ$ from the normal direction toward the transverse direction, neglecting the fact that the point of highest intensity on Fig. 6 is actually inclined $31^\circ$ from the sheet normal and lies slightly off the transverse axis. By comparing the Schmid factors for these axisymmetrically deformed and rolled orientations, it might be possible to predict which composite would have the higher yield strength, phase sizes being equal. Since the ratio of yield strength to UTS displays a consistent proportionality in these materials, one can use Schmid factors to indicate whether UTS will be higher or lower as well, even though, strictly speaking, Schmid factors are predictors of yielding.

As described in the previous section, if Schmid's Law is applied to the $\{10\bar{1}0\}\langle 11\bar{2}0\rangle$ slip system in

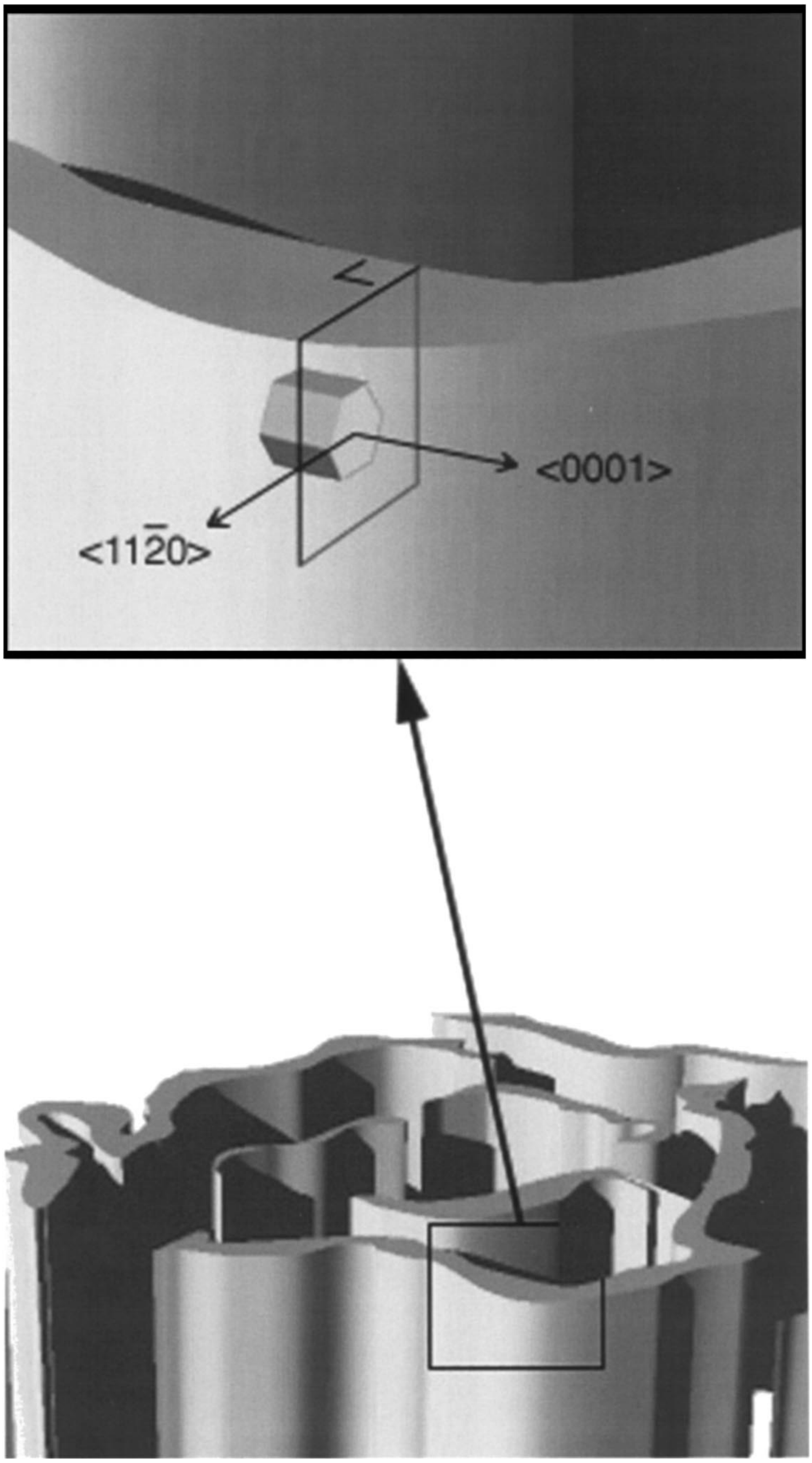

*Figure 9* Oblique view of one HCP phase in a textured axisymmetrically deformed Ti-20Y DMMC with the second HCP phase removed for clarity. (Compare this structure with the microstructure shown in Fig. 2.) The lower illustration shows the convoluted ribbon shape of the microstructure with a rectangle surrounding the region shown in an enlarged view in the upper illustration. The HCP unit cell in the upper view is oriented with the $\langle 10\bar{1}0\rangle$ fiber texture of both the Ti and Y phases as shown in Fig. 8. Note that slip on the $\{10\bar{1}0\}\langle 11\bar{2}0\rangle$ slip system will be constrained to move only in the relatively narrow space between the filament boundaries; slip is not possible parallel to the $\langle 0001\rangle$.

an axisymmetrically deformed composite with the $\langle 1010\rangle$ fiber texture, a resolved shear stress of $0.433\sigma$ is calculated, and the resolved shear stress for basal slip is nil. With the texture observed for Ti in the rolled composite, applying Schmid's Law to calculate the shear stress for basal plane slip is slightly more complicated. A crystal in this orientation has two possible $\langle 1120\rangle$ slip direction positions, each of which is associated with two slip planes. Thus, Schmid factors for four different slip systems need to be calculated, as illustrated in Figs 10 and 11:

$$\begin{aligned}\vec{V}_1 &= \hat{i}\\ \vec{V}_2 &= -0.5\hat{i} + 0.866\hat{j}\\ \vec{V}_{\mathrm{TA}} &= -0.866\hat{i} + 0.5\hat{k}\\ \vec{V}_{\mathrm{IP}} &= 0.5\hat{i} + 0.866\hat{k}\end{aligned}$$

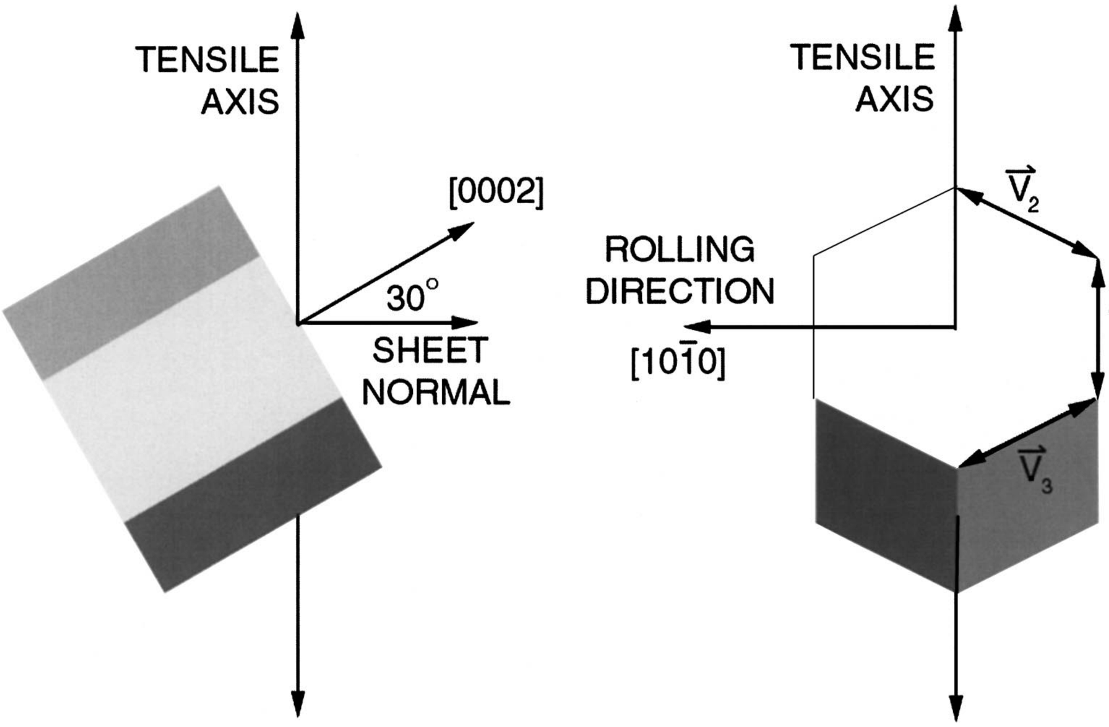

*Figure 10* Depiction of the HCP unit cell orientation in rolled Ti-20Y DMMC. The front view shows an edge view of the (0002) and a true shape view of one {10$\bar{1}$0}-type plane. Note that vectors $\vec{V}_2$ and $\vec{V}_3$ are equivalent for this tensile axis position.

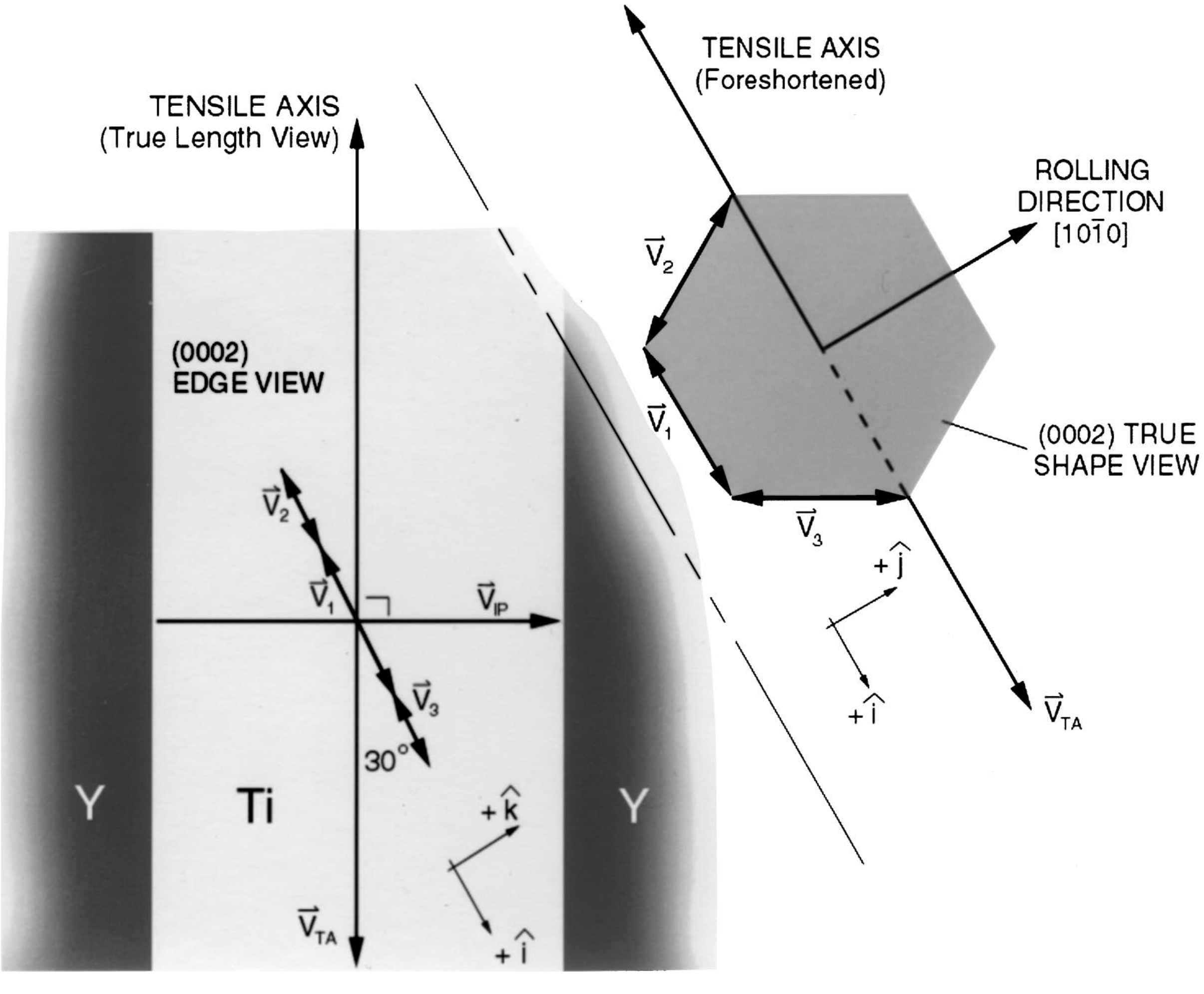

*Figure 11* The HCP unit cell orientation in rolled Ti-20Y DMMC showing the front view and an oblique orthographic projection with the (0002) in true shape. The orientations of the unit vectors $\hat{i}$, $\hat{j}$, and $\hat{k}$ used for all calculations pertaining to the rolled material are shown in both views. A dislocation traveling parallel to $\vec{V}_1$ can travel twice the distance between Y lamellae before encountering a phase boundary; a dislocation traveling parallel to $\vec{V}_2$ or $\vec{V}_3$ can travel four times the distance between Y lamellae before encountering a phase boundary.

$\vec{V}_1$ and $\vec{V}_2$ are $\langle 11\bar{2}0\rangle$ slip directions (note that vector $\vec{V}_3$ marked on Figs 10 and 11 is equivalent to vector $\vec{V}_2$), $\vec{V}_{\mathrm{TA}}$ is the tensile axis, and $\vec{V}_{\mathrm{IP}}$ is the mean perpendicular interlamellar spacing measured from the micrographs. In this study the tensile specimens were cut from the plane of the rolled sheet, such that $\vec{V}_{\mathrm{TA}}$ is perpendicular to $\vec{V}_{\mathrm{IP}}$. For each of the four possible slip systems, the value of cos λ in Schmid's Law can be determined from the dot product of the slip direction vector ($\vec{V}_1$ or $\vec{V}_2$) with $\vec{V}_{\mathrm{TA}}$:

$$\cos\lambda = -0.866 \quad \text{for } \vec{V}_1$$
$$\cos\lambda = 0.433 \quad \text{for } \vec{V}_2$$

The value for cos $\phi$ can be determined from the dot product of the plane normals ($\vec{N}_{\{0002\}}$ or $\vec{N}_{\{10\bar{1}0\}}$) with $\vec{V}_{\mathrm{TA}}$. For example, the cos $\phi$ value for the case of $\vec{V}_2$ lying in the $\{10\bar{1}0\}$:

$$\vec{N}_{\{10\bar{1}0\}} = -0.866\hat{i} - 0.5\hat{j}$$

and

$$\begin{aligned}\vec{N}_{\{10\bar{1}0\}} \cdot \vec{V}_{\mathrm{TA}} &= (-0.866\hat{i} - 0.5\hat{j}) \cdot (-0.866\hat{i} + 0.5\hat{k}) \\ &= \cos\phi\end{aligned}$$

so,

$$\cos\phi = 0.75$$

Performing similar calculations for all four cases yields values for each cos λ and cos $\phi$ term, and these can then be used to calculate the Schmid factor in each case yielding the results shown in Table II.

Since the Ti CRSS in the $\{10\bar{1}0\}\langle 11\bar{2}0\rangle$ is 50 MPa, and the Ti CRSS in the $\{0002\}\langle 11\bar{2}0\rangle$ is 110 MPa, Schmid's Law predicts that the first slip system to move in a tensile specimen of rolled Ti-20Y would be the $\{10\bar{1}0\}\langle 11\bar{2}0\rangle$ where $\vec{V}_2$ is the $\langle 11\bar{2}0\rangle$ slip direction.

$$50\,\mathrm{MPa} = (0.325)\sigma$$
$$\sigma = 154\,\mathrm{MPa}$$

which is less than the basal slip tensile stresses of 254 MPa for $\vec{V}_1$ and 509 MPa for $\vec{V}_2$. The polycrystalline nature of the Ti matrix and the presence of the Y second phase limits the volume of Ti metal that can accept the lattice strain around each dislocation formed at Frank-Read sources, and the work hardening effect of the prior cold work experienced by all specimens in this study will also raise the yield strength; therefore, the actual yield point for rolled Ti-20Y is higher than 154 MPa.

TABLE II Schmid factors for the four slip systems in rolled Ti-20Y tensile specimens assuming all lamellae are oriented with "ideal" texture. $\vec{V}_1$ and $\vec{V}_2$ refer to the $\langle 11\bar{2}0\rangle$ slip directions marked in Figs 10 and 11

| | $\vec{V}_1$ | $\vec{V}_2$ |
|---|---|---|
| {0002} slip plane | 0.433 | 0.216 |
| $\{10\bar{1}0\}$ slip plane | 0 | 0.325 |

When one compares the Schmid factor for easiest slip in the rolled composite ($0.325\sigma$) with that in the axisymmetrically deformed composite ($0.433\sigma$), it seems paradoxical that the Schmid factor should be lower in the rolled composite, because for the case of the best match of equivalent phase sizes, the rolled composite ($\eta = 6.17$) exhibits lower tensile strength than the axisymmetrically deformed composite ($\eta = 5.03$). The explanation for this apparent inconsistency may lie in the fact that the final stages of deformation for both specimens was done by cold work, and thus each composite presumably had relatively high dislocation densities at the start of the tensile tests. The opportunities for "easy slip" would be few in such cold-worked material, with extensive dislocation tangling present from the outset of the tensile test. In such material, the initial plastic flow might be expected to involve cross slip of screw dislocations switching slip planes from the $\{10\bar{1}0\}$ to the {0002}. If this is the case, note that the resolved shear stress on the (0002) planes in the axisymmetrically deformed composite is zero (ideally) or near zero (in actuality), whereas the rolled material has Schmid factors of 0.433 and 0.216 on the (0002) plane. Thus, cross slip would be a feasible mechanism for plastic flow in the rolled composite. In contrast, plastic flow requiring cross slip in the axisymmetrically deformed composite would rely upon the relatively few Ti grains that are oriented at large angles from the orientation of the assumed "ideal texture" or upon twinning in the Ti matrix. Still another factor favoring cross slip in the rolled composite is the presence of a secondary texture in the rolled material corresponding to the area of intensity at $\varphi = 74^\circ$, $\phi = 339^\circ$ in Fig. 6. Grains with this orientation can slip on both the $\{10\bar{1}0\}$ and the (0002) planes, although the Schmid factors for these systems are lower than they are for the primary texture orientation.

Earlier investigators [29–33] of strengthening effects in DMMC's used the spacing between second phase filaments and the thickness of the second phase filaments as key factors in modeling the strength of these materials, but with one exception [29] did not account for crystallographic texture in their models. This study demonstrates that crystallographic texture also plays an important role in determining the ultimate tensile strength of a DMMC. One of the basic precepts of predicting ultimate tensile strength of metals could be summarized as: "the smaller the spacing between dislocation barriers in the microstructure, the stronger the metal." Barriers to dislocation motion include grain boundaries, phase boundaries, and other dislocations.

Many models relating DMMC strength to phase size have assumed that the distance dislocations could travel in the matrix metal was directly proportional to the distance between second phase filaments; however, this assumption neglects the fact that the matrix metal is strongly textured. Texture alters the effective distance dislocations can move by constraining dislocations to follow slip planes that may lie either nearly perpendicular to the filaments or at oblique angles to the filaments, a difference that substantially changes the actual distance a dislocation moves before encountering a barrier.

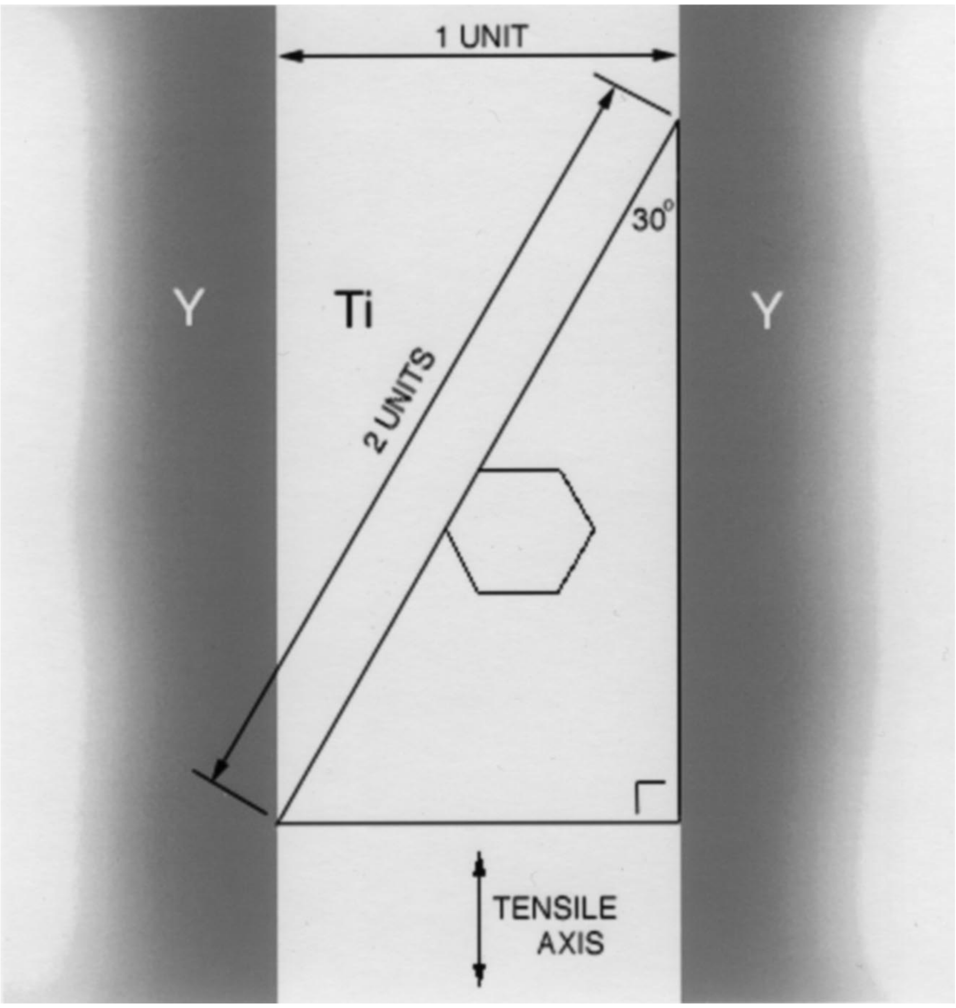

*Figure 12* The $\langle 10\bar{1}0\rangle$ fiber texture of a Ti filament in an axisymmetrically deformed Ti-20Y DMMC constrains slip to a plane segment whose length is twice the thickness of the Ti phase. A dislocation traveling on this plane can travel twice the distance between Y lamellae before encountering a phase boundary.

In axisymmetrically deformed Ti-20Y, the $\langle 10\bar{1}0\rangle$ fiber texture observed for both Ti and Y aligns dislocation Burger's vectors at a 30° angle to the tensile axis. This has the effect of permitting a dislocation to travel twice the distance of the second phase spacing in the matrix before it encounters a phase boundary (Fig. 12).

The geometric possibilities are more numerous in the rolled Ti-20Y composite. There are different angles between the tensile axis and the two $\langle 11\bar{2}0\rangle$ slip directions, $\vec{V}_1$ and $\vec{V}_2$. As shown in Figs 10 and 11, the angles formed by $\vec{V}_1$ and $\vec{V}_2$ with $\vec{V}_{\mathrm{IP}}$ are 60° and 75.5° respectively, as calculated by their unit vector dot products:

$$\begin{gathered}
\vec{V}_1 \cdot \vec{V}_{\mathrm{IP}} = \cos\phi \\
(\hat{\imath}) \cdot (0.5\hat{\imath} + 0.866\hat{k}) = \cos\phi \\
\cos\phi = 0.5 \\
\phi = 60^\circ \\
\vec{V}_2 \cdot \vec{V}_{\mathrm{IP}} = \cos\phi \\
(-0.5\hat{\imath} + 0.866\hat{\jmath}) \cdot (0.5\hat{\imath} + 0.866\hat{k}) = \cos\phi \\
\cos\phi = -0.25 \\
\phi = 75.5^\circ
\end{gathered}$$

Thus, a dislocation moving in the direction of $\vec{V}_1$ can travel twice the distance of the second phase spacing in the matrix before it encounters a phase boundary, and a dislocation moving in the direction of $\vec{V}_2$ can travel four times the distance of the second phase spacing in the matrix before it encounters a phase boundary. This is a large departure from the assumption that the distance between second phase filaments is directly proportional to the distance dislocations can travel in the matrix metal.

These differences in the angles of dislocation travel with the second phase boundaries would be expected to make the rolled Ti-20Y composite ultimate tensile strength lower than that of axisymmetrically deformed Ti-20Y composite of equal phase size. This analysis shows that in rolled Ti-20Y the $\{10\bar{1}0\}\langle 11\bar{2}0\rangle$ slip system has the lowest critical resolved shear stress and is oriented at a 75° angle to the Y lamellae. Both of these factors would make slip easier in rolled Ti-20Y than in axisymmetrically deformed Ti-20Y of equal phase size and spacing. Also contributing to this disparity, the rolled material has readily available secondary slip systems that are absent in the axisymmetrically deformed material, as discussed in the previous section. And indeed, in the Ti-20Y composites of this study, the UTS of cold rolled Ti-20Y ($\eta = 6.17$; Ti phase thickness = 0.56 $\mu$m; UTS = 609 MPa) is lower than the UTS of cold swaged Ti-20Y ($\eta = 5.03$; Ti phase thickness = 0.59 $\mu$m; UTS = 655 MPa), although the magnitude of the difference is modest.

Is this, then, a definitive demonstration of the validity of the texture-microstructure-strength analysis presented in this study? Unfortunately, it is not. The effect of work hardening in the rolled and swaged specimens is difficult to compare directly. It is true that the true strain of the cold rolling from $\eta = 5.28$ to 6.17 is 0.89, and the true strain of the 60% reduction by cold swaging from the previous anneal to $\eta = 5.03$ is 0.91, which makes the amount of cold work approximately equal in terms of true strain. But the dislocation densities present in each specimen before and after cold work are unknown and may have been unequal. Moreover, the analysis presented here implicitly assumes that phase boundaries are effective barriers to dislocation motion. However, in identically textured Ti and Y phases, it may be possible for the strain field surrounding a dislocation traveling through one phase to generate another dislocation with the same orientation in the neighboring HCP phase. The unit cell dimensions are substantially different between Y (atomic radius = 0.181 nm) and Ti (atomic radius = 0.145 nm), but the alignment of slip systems would be favorable for nucleation of new dislocations in the adjacent phase.

### 4.3. Possible future studies to improve the analysis

One possible improvement in experimental methods would be use of induction heating to quickly raise the DMMC billet temperature just a few seconds prior to deformation. This would minimize the coarsening effect from prolonged "soaking" in furnaces prior to and in between deformation passes and might allow production of the sub-50 nm Ti phase thicknesses that $\eta = 6$ should be capable of forming in this composite. This would permit comparison of the rolled Ti-20Y composite properties to those of the axisymmetrically deformed composite at higher $\eta$ values without the uncertainty introduced by the effects of cold work. It might also provide a DMMC sheet of exceptional strength for engineering applications.

## 5. Acknowledgements and intellectual property rights

The authors are grateful to J. D. Verhoeven, R. K. Trivedi, L. L. Jones, L. P. Lincoln, L. K. Reed, J. T. Wheelock, V. Gantovnik, K. Xu and C. F. Burg, all of Ames Laboratory, for their valuable discussions and for preparing the materials used in this study. This work was performed at Ames Laboratory, operated for the U.S. Department of Energy by Iowa State University under contract no. W-7405-ENG-82 and at G & S Titanium, Wooster, OH. Costs of the deformation processing were partially supported by Rohr, Inc., with additional financial support from the U.S. Department of Energy and the Engineering Research Institute of Iowa State University.

Some of the materials and processes described in this article are protected by U.S. patent number 5,200,004 and other patents pending. Licensing inquiries should be directed to Mr. John Weis, Office of Technology Commercialization, 151 ASC II, Iowa State University, Ames, IA 50011.

## References

1. J. BEVK, J. P. HARBISON and J. L. BELL, *J. Appl. Phys.* **49**(12) (1978) 6031.
2. J. D. VERHOEVEN, F. A. SCHMIDT, E. D. GIBSON and W.A. SPITZIG, *J. Metals* **38**(9) (1986) 20.
3. J. D. VERHOEVEN, W. A. SPITZIG, L. L. JONES, H. L. DOWNING, C. L. TRYBUS, E. D. GIBSON, L. S. CHUMBLEY, L. G. FRITZMEIER and G. D. SCHNITTGRUND, *J. Mater. Eng.* **12**(2) (1990) 127.
4. W. A. SPITZIG and P. D. KROTZ, *Acta Met.* **36**(7) (1988) 1709.
5. J. D. VERHOEVEN, W. A. SPITZIG, F. A. SCHMIDT, P. D. KROTZ and E. D. GIBSON, *J. Mater. Sci.* **24** (1989) 1015.
6. P. D. FUNKENBUSCH and T. H. COURTNEY, *Acta Met.* **33**(5) (1985) 913.
7. L. S. CHUMBLEY, H. L. DOWNING, W. A. SPITZIG and J. D. VERHOEVEN, *Mater. Sci. Eng.* **A117** (1989) 59.
8. C. L. TRYBUS, L. S. CHUMBLEY, W. A. SPITZIG and J. D. VERHOEVEN, *Ultramicroscopy* **30** (1989) 315.
9. P. D. FUNKENBUSCH and T. H. COURTNEY, *Scripta Met.* **23** (1989) 1719.
10. W. A. SPITZIG, J. D. VERHOEVEN, C. L. TRYBUS and L. S. CHUMBLEY, *Scripta Met. et Mater.* **24** (1990) 1171.
11. A. M. RUSSELL, L. S. CHUMBLEY, T. W. ELLIS, F. C. LAABS, B. NORRIS and G. E. DONIZETTI, *J. Mater. Sci.* **30** (1995) 4249.
12. J. A. JENSEN, A. M. RUSSELL, T. W. ELLIS and L. S. CHUMBLEY, in "Trace & Reactive Metals: Processing and Technology," edited by R. G. Reddy and B. Mishra (TMS Publications, Warrendale, PA, USA, 1995) p. 508.
13. C. L. H. THIEME, S. POURRAHIMI and S. FONER, *Scripta. Metall. Mater.* **28** (1993) 913.
14. A. M. RUSSELL, T. LUND, L. S. CHUMBLEY, F. C. LAABS, L. L. KEEHNER and J. L. HARRINGA, Composites: Part A (accepted, in press).
15. A. M. RUSSELL, Y. TIAN, J. D. ROSE, T. W. ELLIS and L. S. CHUMBLEY, *J. Mater. Res.* (accepted, in press).
16. A. M. RUSSELL, L. S. CHUMBLEY, J. E. PARKS and K. XU, Gold Bulletin (accepted, in press).
17. C. A. TRYBUS, PhD Dissertation, Iowa State University, 1988.
18. D. N. WILLIAMS and D. S. EPPELSHEIMER, *Nature* **170** (1952) 146.
19. G. Y. CHIN, "ASM Metals Handbook," Vol. 8 (ASM International, Materials Park, OH, USA, 1985) p. 229.
20. E. A. ANDERSON, D. C. JILLSON and S. R. DUNBAR, *J. Metals Trans. AIME* **197** (1953) 1191.
21. T. E. SCOTT, in "Handbook on the Physics and Chemistry of the Rare Earths: Volume 1 - Metals," edited by K. A. Gschneidner, Jr. and L. R. Eyring (North-Holland Publishing, Amsterdam, 1978) p. 608.
22. E. E. UNDERWOOD, "Quantitative Stereology" (Addison-Wesley, 1970) Chaps. 3, 4.
23. J. C. MALZAHN KAMPE, T. H. COURTNEY and Y. LENG, *Acta Metall.* **37**(7) (1989) 1735.
24. T. H. COURTNEY and J. C. MALZAHN KAMPE, *ibid.* **37**(7) (1989) 1747.
25. D. G. MORRIS and M. A. MORRIS, *Acta Metall. Mater.* **39**(8) (1991) 1763.
26. O. N. CARLSON, D. W. BARE, E. D. GIBSON and F. A. SCHMIDT, Symposium on Newer Metals: Special Technical Publication No. 272 (American Society for Testing Materials, 1959) p. 144.
27. M. J. DONACHIE, Jr., "Titanium: A Technical Guide" (ASM International, Materials Park, OH, USA, 1988) pp. 40–41.
28. A. I. PIKALOV, V. V. VOROB'YEV, I. I. PAPIROV and A. S. KAPCHERIN, *Izv. Akad. Nauk. SSSR, Metally.* **4** (1983) 153.

29. J. D. EMBURY and R. M. FISHER, *Acta Metall.* **14** (1966) 147.
30. M. A. MORRIS and D. G. MORRIS, *Mater. Sci. Eng.* **A111** (1989) 115.
31. E. OROWAN, Symposium on Internal Stresses in Metals and Alloys; Discussion, Monograph, and Report Series No. 5 (Inst. of Metals, London, 1948) p. 451.
32. J. G. SEVILLANO, in “Strength of Metals and Alloys,” Proc. ICSMA 5th edited by P. Haasen, V. Gerold, and G. Kowtorz (Pergamon Press, Oxford, 1980) p. 819.
33. J. D. VERHOEVEN, L. S. CHUMBLEY, F. C. LAABS, and W. A. SPITZIG, *Acta Metall.* **39** (1991) 2825.

*Received 24 August*
*and accepted 13 October 1998*